nature chemistry

Article

https://doi.org/10.1038/s41557-023-01356-1

Superstructural ordering in self-sorting coacervate-based protocell networks

Received: 24 November 2022

Accepted: 27 September 2023

Wenjing Mu [1,2,8], **Liyan Jia** [1,2,8], **Musen Zhou** [3], **Jianzhong Wu** [3], **Yiyang Lin** [4] ✉, **Stephen Mann** [5,6,7] ✉ & **Yan Qiao** [1,2] ✉

Bottom-up assembly of higher-order cytomimetic systems capable of coordinated physical behaviours, collective chemical signalling and spatially integrated processing is a key challenge in the study of artificial multicellularity. Here we develop an interactive binary population of coacervate microdroplets that spontaneously self-sort into chain-like protocell networks with an alternating sequence of structurally and compositionally dissimilar microdomains with hemispherical contact points. The protocell superstructures exhibit macromolecular self-sorting, spatially localized enzyme/ribozyme biocatalysis and interdroplet molecular translocation. They are capable of topographical reconfiguration using chemical or light-mediated stimuli and can be used as a micro-extraction system for macroscale biomolecular sorting. Our methodology opens a pathway towards the self-assembly of multicomponent protocell networks based on selective processes of coacervate droplet–droplet adhesion and fusion, and provides a step towards the spontaneous orchestration of protocell models into artificial tissues and colonies with ordered architectures and collective functions.

Organization of artificial cell-like compartments (protocells) into interconnected protocell networks provides opportunities to study aspects of artificial multicellularity such as long-range programmable signalling[1], controlled protein expression[2], morphogen-mediated differentiation[3] and utilization of externally stored energy[4]. Building higher-order cytomimetic systems is timely because numerous protocell models are currently available, including lipid vesicles[5–7], polymersomes[8,9], proteinosomes[10], colloidosomes[11–13], polysaccharidosomes[14,15] and membraneless[16,17] or membranized[18–21] coacervate microdroplets. These synthetic constructs exhibit a diversity of life-like properties such as cell-free gene expression[22]; DNA transcription[23,24]; growth, division and fusion[25–27]; biochemical activity[28–31]; sensing and motility[32,33]; phagocytosis[34]; and predation[35,36], which are associated with the endogenous activity of discrete protocells or their contact-dependent interactivity. Extending these attributes into higher-order networks necessitates the controlled assembly and ordering of protocell populations in space and time[37], and has been achieved principally through the use of external manipulation involving 3D printing[38–40], acoustic force fields[41], magnetic fields[42] micropipetting[43] and microfluidics[44,45]. By contrast, although randomly organized tissue-like colonies of protocells have been prepared using interfacial click chemistry[46,47] or hydrogel immobilization[48], the spontaneous bottom-up assembly of organized protocell networks without external manipulation or energy input (for example, through the use of programmable DNA interactions[49,50]) remains a considerable challenge.

---

[1] Beijing National Laboratory for Molecular Sciences (BNLMS), Laboratory of Polymer Physics and Chemistry, CAS Research/Education Center for Excellence in Molecular Sciences, Institute of Chemistry, Chinese Academy of Sciences, Beijing, China. [2] University of Chinese Academy of Sciences, Beijing, China. [3] Department of Chemical and Environmental Engineering, University of California, Riverside, CA, USA. [4] State Key Laboratory of Chemical Resource Engineering, Beijing Laboratory of Biomedical Materials, Beijing University of Chemical Technology, Beijing, China. [5] Centre for Protolife Research and Centre for Organized Matter Chemistry, School of Chemistry, University of Bristol, Bristol, UK. [6] Max Planck-Bristol Centre for Minimal Biology, School of Chemistry, University of Bristol, Bristol, UK. [7] School of Materials Science and Engineering, Shanghai Jiao Tong University, Shanghai, P. R. China. [8] These authors contributed equally: Wenjing Mu, Liyan Jia. ✉e-mail: y.lin@mail.buct.edu.cn; S.Mann@bristol.ac.uk; yanqiao@iccas.ac.cn

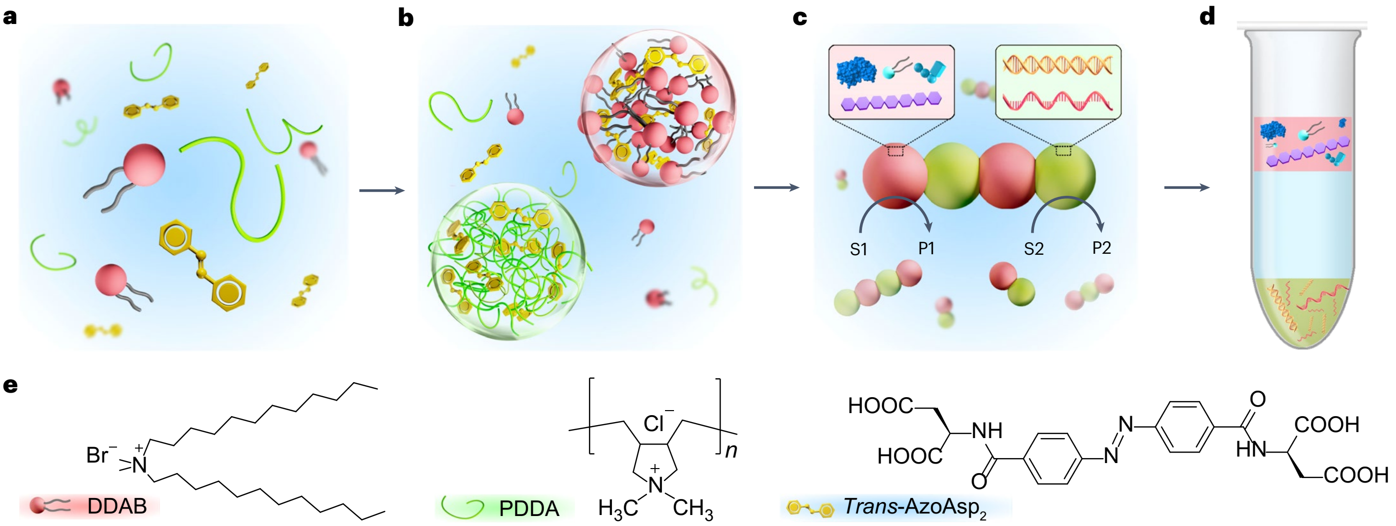

Fig. 1 | Spontaneous assembly, spatial segregation, self-organization and macroscopic sorting of coacervate-based protocell networks. **a,b**, Mixing of DDAB (red), PDDA (green) and *trans*-AzoAsp$_2$ (yellow) (**a**) results in associative LLPS and spontaneous spatial segregation to give a binary population of immiscible DDAB/*trans*-AzoAsp$_2$ and PDDA/*trans*-AzoAsp$_2$ coacervate microdroplets (**b**). **c**, Localized self/non-self adhesion and self/self fusion within mixed-droplet aggregates produces self-organized chain-like networks with an alternating sequence of interconnected droplets and contiguous hemispherical contacts. Biomolecules are selectively partitioned within the DDAB/*trans*-AzoAsp$_2$ (red) and PDDA/*trans*-AzoAsp$_2$ (green) coacervate droplets to generate integrated higher-order protocell assemblies capable of macromolecular self-sorting, spatially localized biocatalysis (substrate S1/product P1 and S2/P2) and interdroplet molecular transfer. The networks are reconfigured by chemical or photochemical stimuli. **d**, Centrifugation of the protocell networks results in biomolecular extraction and macroscopic sorting via a three-layer separation process: DDAB/*trans*-AzoAsp$_2$ (upper layer), depleted aqueous phase (middle layer) and PDDA/*trans*-AzoAsp$_2$ (lower layer). **e**, Molecular structures of DDAB, PDDA and *trans*-AzoAsp$_2$.

In this work we report the self-organization of reconfigurable chain-like protocell networks capable of macromolecular self-sorting, spatially localized biocatalysis and interdroplet molecular translocation (Fig. 1). We show that associative liquid–liquid phase separation (LLPS) in a ternary mixture of a double-tailed quaternary cationic amphiphile (didodecyldimethyl ammonium bromide, DDAB), a cationic polyelectrolyte (poly(diallyldimethylammonium chloride, PDDA, 100–200 kDa; polymerization degree ≈ 620–1,240) and a photoactive anionic aspartic-acid-appended azobenzene derivative (*trans*-AzoAsp$_2$, Supplementary Fig. 1) produces a binary population of immiscible DDAB/*trans*-AzoAsp$_2$ and PDDA/*trans*-AzoAsp$_2$ coacervate microdroplets with liquid crystalline and homogeneous internal structures, respectively. The coacervate droplets spontaneously self-organize into linear and branched chains with an alternating sequence of structurally dissimilar microdomains and hemispherical contact junctions. By recruiting different biomacromolecules into specific domains of the protocell superstructure, we implement spatially localized enzyme- or ribozyme-mediated reactions within the self-assembled networks. The chain-like arrays can be topologically reconfigured by selective domain disassembly arising from host–guest complexation of β-cyclodextrin (β-CD)[51] within the DDAB/*trans*-AzoAsp$_2$ coacervate droplets, or by differential stabilities in the presence of sodium chloride. Alternatively, fusion of the immiscible coacervate droplets within the networks and reversible transfer of guest molecules can be induced by photoisomerization of AzoAsp$_2$ (ref. 52). Finally, we develop a protocell network-based micro-extraction and macroscale biomolecular sorting system by exploiting differences in coacervate density to release and separate the interconnected droplets and their constituent macromolecular cargoes. Taken together, our results demonstrate that superstructural ordering of dissimilar coacervate droplets can be achieved spontaneously by selective droplet–droplet adhesion and fusion, which opens a pathway to the self-assembly of multicomponent protocell networks and provides a step towards higher-order cytomimetic systems capable of selective sorting and spatially integrated chemical processing.

Results and discussion

Protocell network components and assembly

We prepared populations of immiscible DDAB/*trans*-AzoAsp$_2$ and PDDA/*trans*-AzoAsp$_2$ coacervate droplets as the basis for constructing a higher-order multicomponent protocell network. First we investigated the individual coacervate systems before self-assembly. In both cases, mixing aqueous solutions of DDAB or PDDA with *trans*-AzoAsp$_2$ at a DDAB/*trans*-AzoAsp$_2$ or PDDA/*trans*-AzoAsp$_2$ molar ratio of 4:1 gave rise to positively charged coacervate microdroplets (typical zeta potentials: +37 mV for DDAB/*trans*-AzoAsp$_2$ and +8 mV for PDDA/*trans*-AzoAsp$_2$), which were usually <10 μm in diameter (mean diameters: 2.1 μm (DDAB/*trans*-AzoAsp$_2$); 2.8 μm (PDDA/*trans*-AzoAsp$_2$)). The DDAB/*trans*-AzoAsp$_2$ coacervate droplets were readily imaged by fluorescence microscopy using the hydrophobic fluorophore, Nile red, which was sequestered into the coacervate phase (Fig. 2a). Polarized optical microscopy (POM) images on single droplets showed intense birefringent Maltese cross-patterns (Fig. 2b) that disappeared after incubation at 90 °C for 15 min, which is indicative of a liquid crystalline DDAB/*trans*-AzoAsp$_2$ coacervate[53]. Conversely, the PDDA/*trans*-AzoAsp$_2$ droplets preferentially accumulated hydrophilic fluorophores such as 8-hydroxypyrene-1,3,6-trisulfonic acid (HPTS) and showed no birefringence (Fig. 2c,d), indicating a homogeneous coacervate matrix with a relatively high dielectric constant. Small- and wide-angle X-ray scattering (SAXS and WAXS) profiles of the DDAB/*trans*-AzoAsp$_2$ coacervate showed a strong *d*-spacing at 2.70 nm and 2.63 nm, respectively, corresponding to approximately twice the length of the DDAB molecule, and consistent with ordered packing of the alkyl chains of the amphiphile in the liquid crystalline phase. By contrast, no reflection peaks were observed for the PDDA/*trans*-AzoAsp$_2$ coacervate, which is indicative of a disordered internal structure (Supplementary Fig. 2). This was attributed to random packing of the flexible cationic PDDA chains when electrostatically associated with AzoAsp$_2$ during LLPS. Fluorescence recovery after photobleaching (FRAP) measurements[54] showed slow

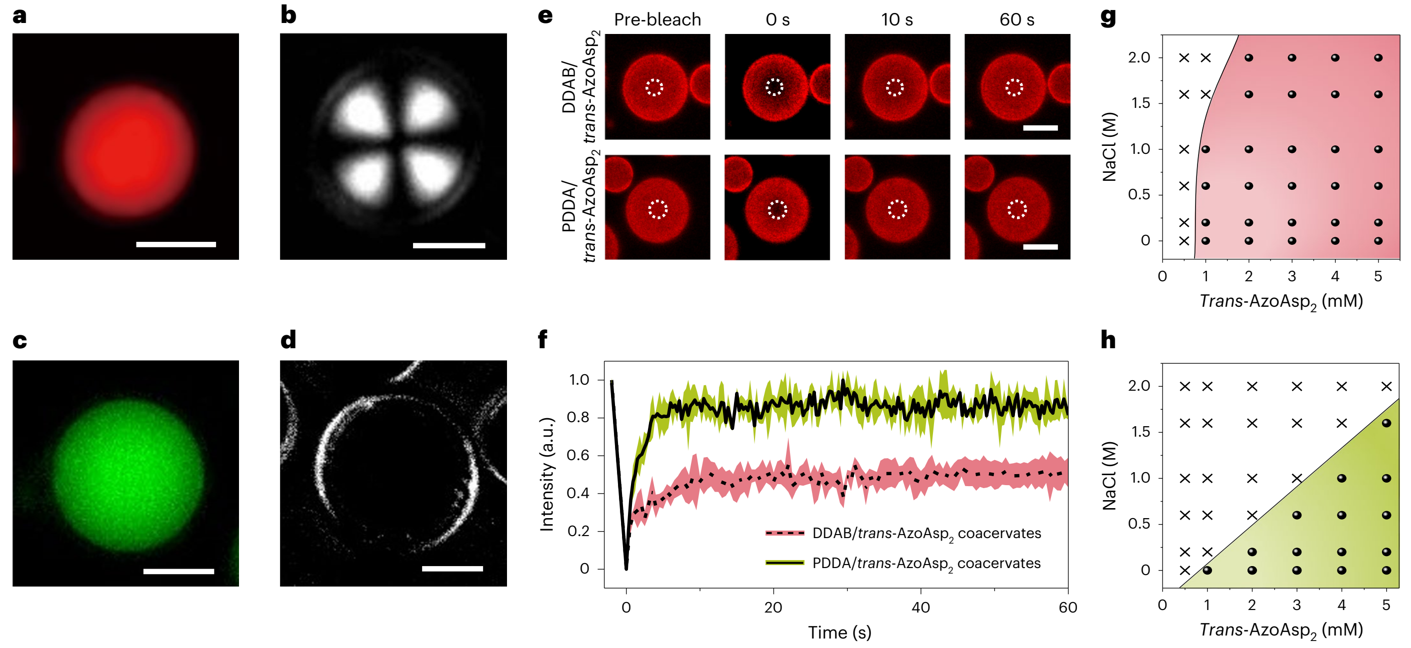

Fig. 2 | Protocell network components. a,b, Fluorescence microscopy (**a**) and optical polarized microscopy (**b**) images of DDAB/*trans*-AzoAsp$_2$ coacervate droplets (molar ratio = 4:1; Nile red hydrophobic stain, red fluorescence). A birefringent Maltese cross-pattern is shown in **b**, indicating liquid crystalline order. **c,d**, Fluorescence microscopy (**c**) and polarized microscopy (**d**) images of PDDA/*trans*-AzoAsp$_2$ coacervate droplets (molar ratio = 4:1; hydrophilic HPTS, green fluorescence). No internal order is observed. **e,f**, FRAP monitoring of fluorescently labelled BSA in coacervate droplets. Time-dependent fluorescence microscopy images (**e**) and corresponding kinetics of fluorescence recovery (**f**) of RITC-BSA-loaded DDAB/*trans*-AzoAsp$_2$ and PDDA/*trans*-AzoAsp$_2$ coacervate droplets; the data are consistent with liquid crystalline and homogeneous coacervate structures, respectively. The data represent mean ± s.d. of three replicates. Scale bars, **a**–**e**, 5 µm. **g,h**, Phase diagrams for DDAB/*trans*-AzoAsp$_2$ (**g**) and PDDA/*trans*-AzoAsp$_2$ (**h**) mixtures prepared in the absence/presence of NaCl. Shaded regions denote conditions under which coacervate microdroplets were observable. Liquid crystalline DDAB/*trans*-AzoAsp$_2$ droplets remain intact in the presence of 2 M sodium chloride, whereas the more hydrophilic PDDA/*trans*-AzoAsp$_2$ droplets disassemble under the same conditions. Concentrations: DDAB (4 mM), PDDA (4 mM), *trans*-AzoAsp$_2$ (0.5–5 mM) and NaCl (0–2 M).

(50% recovery within 10 s) and fast (85% recovery within 5 s) fluorescence recovery in rhodamine isothiocyanate-labelled bovine serum albumin (RITC-BSA)-loaded DDAB/*trans*-AzoAsp$_2$ and PDDA/*trans*-AzoAsp$_2$ coacervate droplets, respectively (Fig. 2e,f), with corresponding estimated apparent diffusion coefficients of 1.1×10^{-13} and 3.9×10^{-13} $m^2 s^{-1}$, respectively[55]. The approximately threefold increase in fluorophore mobility within the PDDA/*trans*-AzoAsp$_2$ microdroplets was attributed to the restricted lateral diffusion of RITC-BSA in the liquid crystalline matrix of the DDAB/*trans*-AzoAsp$_2$ phase. This was consistent with FRAP experiments in which a double-tailed lipid (1,1′-dioctadecyl-3,3′-oxacarbocyanine, DiO) or RITC-labelled PDDA were used as fluorescence probes to determine the diffusivities of the lipid and polyelectrolyte constituents of the coacervate droplets, respectively (Supplementary Fig. 3). Fluorescence recovery of DiO was prohibited in DDAB/*trans*-AzoAsp$_2$ coacervate droplets, whereas fluorescence recovery of RITC-labelled PDDA in PDDA/*trans*-AzoAsp$_2$ coacervates was achieved within 10 s. Further experiments indicated that the increased hydrophobicity of the liquid crystalline DDAB/*trans*-AzoAsp$_2$ phase increased the stability of the droplets against salt-induced dissolution (Fig. 2g,h).

Spontaneous assembly of ordered protocell networks was achieved by mixing DDAB, PDDA and *trans*-AzoAsp$_2$ at a corresponding molar ratio of 4:4:2, at room temperature, for 50 min. Fluorescence microscopy images showed predominantly self-organized superstructures in the form of linear and branched chain-like networks consisting of an alternating sequence of interconnected DDAB/*trans*-AzoAsp$_2$ and PDDA/*trans*-AzoAsp$_2$ coacervate microdroplets (Fig. 3a and Supplementary Fig. 4). Interconnected protocell networks were observed after 4 h incubation (Supplementary Fig. 5). The immiscible droplets adhered to each other with distinct hemispherical contact points to mainly produce linear chains with an average length of 6.3 µm (Supplementary Figs. 6 and 7). Fluorescence intensity profiles along the chains (Supplementary Fig. 8), as well as POM images (Supplementary Fig. 9) and FRAP measurements (Supplementary Fig. 10), confirmed the alternating positioning of the different droplets. Self-sorting of the higher-order superstructures was observed irrespective of the order in which DDAB, PDDA and *trans*-AzoAsp$_2$ were added (Supplementary Fig. 11). We also prepared PDDA/*trans*-AzoAsp$_2$ coacervate droplets using different PDDA molecular weights (<100 kDa, 200–350 kDa and 400–500 kDa) and investigated their spontaneous self-organization in the presence of DDAB/*trans*-AzoAsp$_2$ coacervate droplets. In each case, chain-like networks were observed, indicating that polymer length did not greatly influence the assembly of the protocell superstructures (Supplementary Fig. 12).

Time-dependent plots of forward-light-scattered area (FSC-A) versus side-light-scattered area (SSC-A) derived from fluorescence-activated cell sorting measurements over 90 min showed the progressive emergence of a peak in the maximum FSC-A count (Fig. 3b–e), which was attributed to increasing numbers of chain-like assemblies. The mechanism of chain ordering was monitored using time-lapse fluorescence microscopy. Upon mixing of DDAB, PDDA and *trans*-AzoAsp$_2$, attractive interactions between the DDAB/*trans*-AzoAsp$_2$ and PDDA/*trans*-AzoAsp$_2$ coacervate droplets gave rise to pairwise combinations and small partially organized clusters that increased in length and droplet size, typically over a period of 1 h (Supplementary Fig. 13 and Supplementary Video 1). Ordering within the networks increased with time due to intracluster fusion events, which specifically merged droplets of the same type that were sufficiently close to each other, leaving only a regularly interspersed arrangement of self/non-self cohesive connections (Fig. 3f–i).

Alternate positioning of the DDAB/*trans*-AzoAsp$_2$ and PDDA/*trans*-AzoAsp$_2$ coacervate droplets was most prominent in networks produced when the number density of both types of droplets was approximately equal (DDAB:PDDA = 1:1) (Fig. 3j). Under these conditions, the rates of self/non-self droplet adhesion and self/self droplet coalescence in the initially formed clusters were effectively matched so that regular interspersing of discrete coacervate droplets gave rise to a relatively stable microstructure. In contrast, non-stoichiometric DDAB:PDDA ratios gave rise to the spontaneous assembly of core–satellite droplet clusters (Fig. 3j and Supplementary Fig. 14).

The relative interfacial tensions (γ_{DDAB}, γ_{PDDA} and $\gamma_{\mathrm{DDAB/PDDA}}$) at the coacervate droplet junctions and the corresponding three-phase contact angles (θ_{DDAB} and θ_{PDDA}; $\theta = 180°$ (complete dewetting)) between the microdroplets were determined by image analysis of the fluorescence microscopy images (Fig. 3k)[56,57]. The θ_{DDAB} values determined for different DDAB:PDDA molar ratios remained within a relatively narrow range (135–150°), whereas θ_{PDDA} was smaller and dependent on the DDAB:PDDA molar ratio (Fig. 3l). Specifically, a maximum θ_{PDDA} value of 125° was measured at a DDAB:PDDA molar ratio of 1:1, corresponding to stable alternating sequences of interconnected coacervate droplets. Lower θ_{PDDA} angles ranging from 115° to 55° were observed at molar ratios higher or lower than 1:1 DDAB:PDDA (Fig. 3l), consistent with increased levels of wetting at the droplet junctions. Notably, the DDAB/*trans*-AzoAsp$_2$ droplets were relatively unperturbed on contact with the PDDA/*trans*-AzoAsp$_2$ domains ($\theta_{\mathrm{DDAB}} > \theta_{\mathrm{PDDA}}$), implying that $\gamma_{\mathrm{DDAB/PDDA}}$ was higher than both γ_{DDAB} and γ_{PDDA}, which is consistent with the liquid crystalline structure of the DDAB/*trans*-AzoAsp$_2$ droplets.

Biomolecular organization and processing in protocell networks

Given that alternating sequences of immiscible and structurally dissimilar coacervate droplets could be spontaneously interconnected within chain-like arrays, we sought to use the networks as a platform for constructing a functional multicomponent protocell model with higher-level organization. Based on their distinct composition and structuration, we reasoned that the immiscible coacervate droplets would be able to preferentially sequestrate different biomolecules from the external environment, thereby providing a mechanism for spatially selective molecular partitioning, leading to protocell networks with regiospecific properties and localized chemical processing (Fig. 4a). We tested the selectivity of biomolecular uptake by exposing the coacervate droplet superstructures to mixtures of fluorescently labelled proteins, oligonucleotides and lipids and monitoring the spatial distribution of the guest molecules by fluorescence microscopy. Images recorded using mixtures of RITC-modified horseradish peroxidase (RITC-HRP) and carboxyfluorescein-modified single-stranded DNA (FAM-ssDNA) exhibited high levels of spatial sorting within the networks, with RITC-HRP or FAM-ssDNA distributed preferentially in the DDAB/*trans*-AzoAsp$_2$ or PDDA/*trans*-AzoAsp$_2$ coacervate droplets, respectively (Fig. 4b,c). Similarly, binary mixtures of oligonucleotides and polysaccharides (ssDNA/diethylaminoethyl (DEAE)-dextran; RNA/dextran; ssDNA/heparin; RNA/heparin), lipids (ssDNA/DiO; RNA/DiO), proteins (RNA/HRP) or co-factors (ssDNA/ATP) indicated that DEAE-dextran, DiO, ATP and heparin were preferentially enriched in the DDAB/*trans*-AzoAsp$_2$ domains, whereas ssDNA and RNA oligonucleotides were located primarily in the PDDA/*trans*-AzoAsp$_2$ regions of the protocell networks (Supplementary Figs. 15–17). We attributed the selective partitioning to differences in the internal structure and hydrophilicity of the two coacervate phases. Although multivalent charge interactions facilitated the high solubility of nucleic acid polyanions in PDDA/*trans*-AzoAsp$_2$, the more amphiphilic environment of liquid crystalline DDAB/*trans*-AzoAsp$_2$ was conducive to higher uptake levels of proteins, polysaccharides, lipids and ATP. Selective partitioning was independent of the fluorophores used to label the guest biomolecules (Supplementary Fig. 18).

The self-sorting of biomacromolecules into discrete domains of the chain-like arrays was exploited as a mechanism for undertaking spatially localized enzyme and ribozyme transformations in the protocell networks (Fig. 4d). For example, selective loading of HRP and Amplex red into the DDAB/*trans*-AzoAsp$_2$ domains, followed by addition of hydrogen peroxide converted the substrate into resorufin, resulting in increasing levels of homogeneous red fluorescence specifically in the liquid crystalline coacervate droplets over a period of 500 s (Fig. 4e,f, Supplementary Fig. 19 and Supplementary Video 2). The emission intensity from the DDAB/*trans*-AzoAsp$_2$ domains was 32-fold higher than that measured in the adjacent PDDA/*trans*-AzoAsp$_2$ droplets, indicating a high level of product retention in the HRP-containing reaction environment. By contrast, RNA enrichment and catalysis specifically within the PDDA/*trans*-AzoAsp$_2$ domains was achieved by selective uptake of a minimal hammerhead ribozyme (HH-min) hybridized to a fluorescence resonance energy transfer (FRET) substrate[29]. Cleavage of the FRET-substrate strand by HH-min liberated the fluorophore (6-carboxyfluorescein) from the quencher strand, resulting in an increase in green fluorescence intensity in the PDDA/*trans*-AzoAsp$_2$ coacervate droplets with minimal transfer into the adjacent DDAB/*trans*-AzoAsp$_2$ domains (Fig. 4g,h).

As the above transformations did not involve notable changes in polarity between the reactants and products, substantial transfer of the latter between the different types of droplets was not observed. We conjectured that the fluid-like properties of the DDAB/*trans*-AzoAsp$_2$ and PDDA/*trans*-AzoAsp$_2$ coacervate droplets should facilitate the migration of encapsulated biomolecules between different domains in the protocell superstructures if the guest solubility in the receiver droplets was energetically favoured. To generate non-equilibrium conditions in the protocell network, ssDNA was initially sequestered into a single population of DDAB/*trans*-AzoAsp$_2$ droplets prior to addition of a suspension of PDDA/*trans*-AzoAsp$_2$ droplets and formation of the protocell chains. Localized self/non-self adhesion within the regularly interspersed arrays then gave rise to contact-dependent transfer of the ssDNA from the PDDA/*trans*-AzoAsp$_2$ domains into adjacent DDAB/*trans*-AzoAsp$_2$ droplets (Fig. 4i). To validate this hypothesis, we pre-loaded carboxytetramethylrhodamine (TAMRA)-ssDNA into DDAB/*trans*-AzoAsp$_2$ droplets, added PDDA/*trans*-AzoAsp$_2$ droplets to generate the protocell chains, and monitored the interdroplet mobility of the oligonucleotide by recording the changes in fluorescence intensity in adjacent droplets (Fig. 4j and Supplementary Video 3). Typically,

Fig. 3 | Protocell network assembly. **a**, Fluorescence microscopy image showing linear and branched chain-like assemblies of alternating Nile-red-loaded DDAB/*trans*-AzoAsp$_2$ (red fluorescence) and HPTS-loaded PDDA/*trans*-AzoAsp$_2$ (green fluorescence) interconnected coacervate microdroplets (DDAB:PDDA:*trans*-AzoAsp$_2$ molar ratio = 4:4:2). **b**–**d**, Fluorescence-activated cell-sorting time-series of FSC-A versus SSC-A dot plots for co-existing DDAB/*trans*-AzoAsp$_2$ and PDDA/*trans*-AzoAsp$_2$ coacervate droplets after mixing in the dark (t_0) (**b**), at t_0 + 30 min (**c**) and at t_0 + 90 min (**d**). Formation of the chain-like assemblies after 30 min gives rise to a specific increase in scattering (red domain) in a localized region of the pseudo-colour plots ($n = 100{,}000$). **e**, Corresponding plots of counts against FSC-A values at different times. **f**–**i**, Time-series of fluorescence microscopy images showing spontaneous self/non-self droplet adhesion (white arrows in **f** and **g**) and self/self droplet fusion (red and green arrows in **g** and **h**) to produce a stabilized chain with alternating DDAB/*trans*-AzoAsp$_2$ (red) and PDDA/*trans*-AzoAsp$_2$ (green) coacervate droplets (**i**). **j**, Protocell network assembly at DDAB:PDDA molar ratios of 1:0.2, 1:0.5, 1:1, 1:2, 1:3 and 1:4 showing optimal matching for linear chain formation at 1:1, and core–satellite arrangements under non-stoichiometric conditions. Staining as in **a**. **k**,**l**, Graphics showing contact points associated with interfacial tensions (γ_{DDAB}, γ_{PDDA} and $\gamma_{\mathrm{DDAB/PDDA}}$) and contact angles ($\theta_{\mathrm{DDAB}}$ and θ_{PDDA}) (**k**), and plots of (θ_{DDAB} and θ_{PDDA}) against DDAB/PDDA molar ratio (**l**). The data represent mean ± s.d. of three replicates. Scale bars, **a**, 10 μm; **f**–**j**, 5 μm.

https://doi.org/10.1038/s41557-023-01356-1

95% of the TAMRA-ssDNA pre-loaded into the DDAB/*trans*-AzoAsp$_2$ domains was transferred into adjacent PDDA/*trans*-AzoAsp$_2$ droplets within 8 min (Fig. 4k), confirming that molecular transfer was possible under non-equilibrium conditions.

Stimuli-induced reconfiguration in protocell networks

We investigated three mechanisms for controlling the topographical reconfiguration of the chain-like superstructures as a step towards triggering the transfer and redistribution of guest molecules from

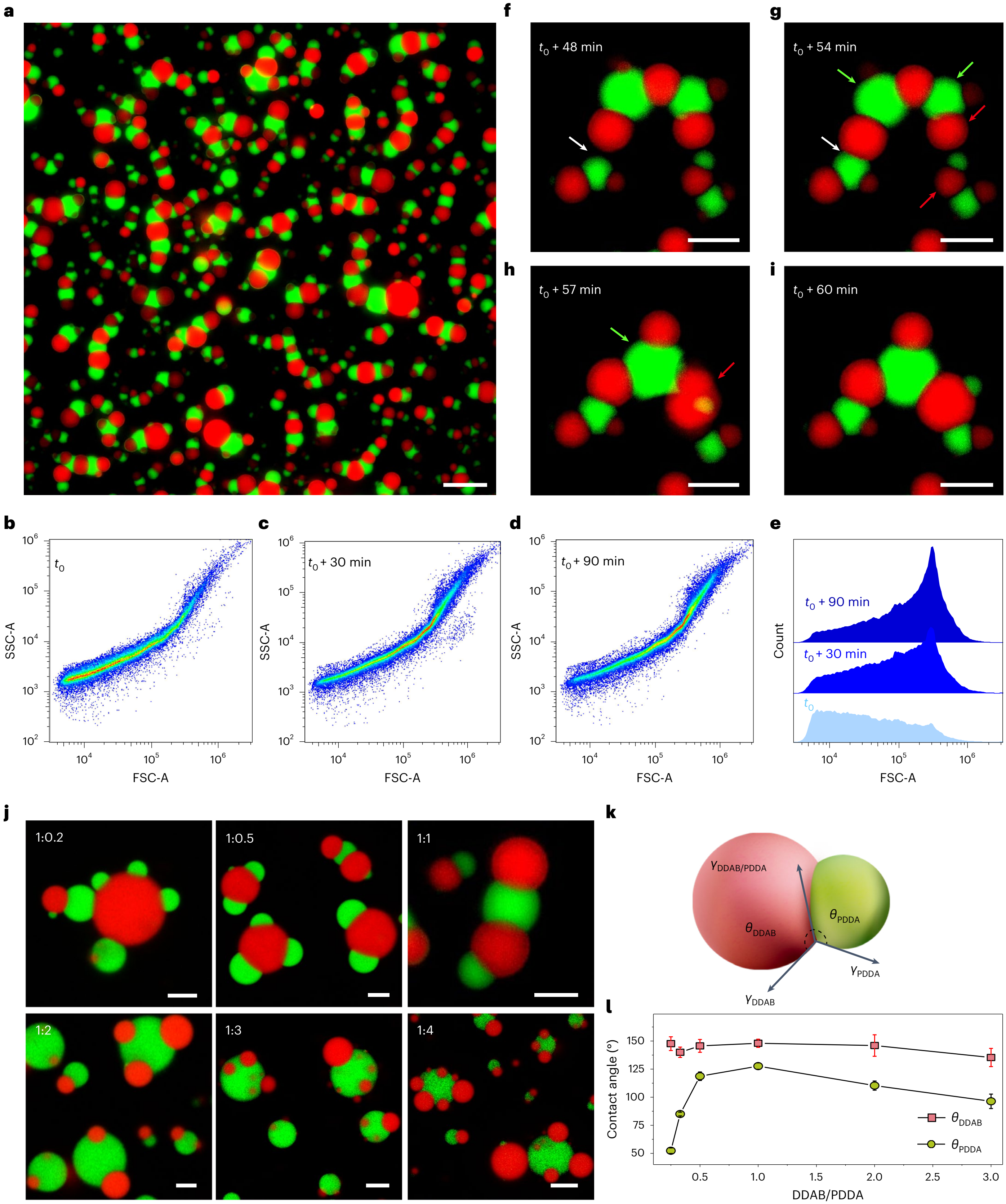

https://doi.org/10.1038/s41557-023-01356-1

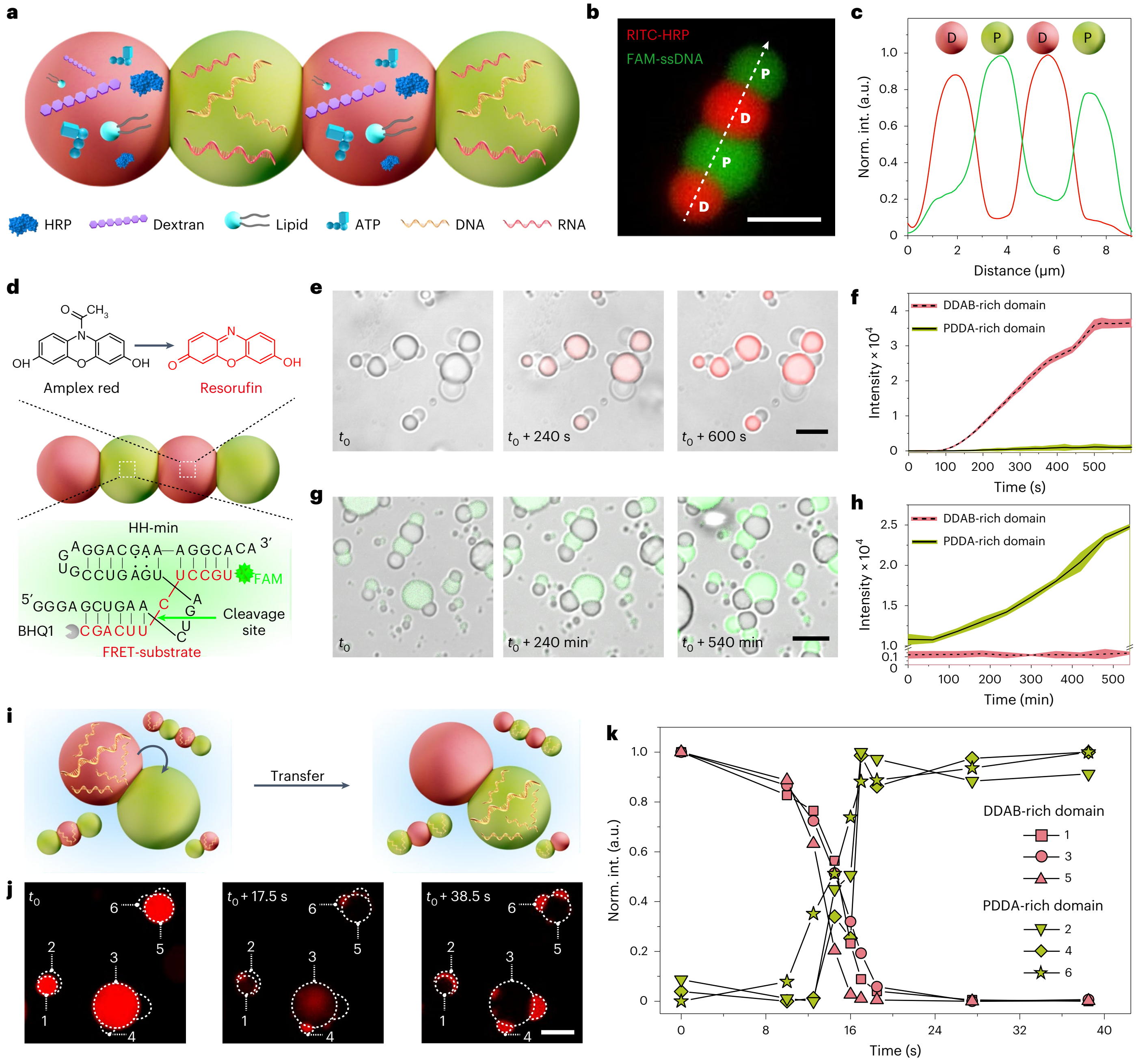

Fig. 4 | Biomolecular organization and processing in protocell networks. **a**, Graphical illustration showing a higher-order multicomponent protocell model. Spontaneous self-sorting of enzymes (HRP), polysaccharides (dextran), lipids (DiO), co-factors (ATP) and single-stranded polynuclotides (DNA and RNA) in linked chains of alternating DDAB/*trans*-AzoAsp$_2$ (red) and PDDA/*trans*-AzoAsp$_2$ (green) coacervate microdroplets occurs by spatially selective molecular partitioning, leading to regiospecific properties and chemical processing. **b**, Fluorescence microscopy image of a single chain of regularly interspersed DDAB/*trans*-AzoAsp$_2$ (**D**) and PDDA/*trans*-AzoAsp$_2$ (**P**) coacervate microdroplets showing selective partitioning of RITC-HRP (red fluorescence) and FAM-ssDNA (green fluorescence) in the **D** and **P** domains, respectively, of the interconnected network. **c**, Corresponding fluorescence intensity line profile (dashed line in **b**) showing alternating sequence of RITC-HRP (red line) and FAM-ssDNA (green line) enriched specifically in the **D** and **P** droplets, respectively. **d**, Schematic showing spatially organized biomolecular processing in protocell networks. Enzyme (HRP) or ribozyme (HH-min) transformations occur in an alternating sequence of interconnected DDAB/*trans*-AzoAsp$_2$ (red) and PDDA/*trans*-AzoAsp$_2$ (green) coacervate microdroplets. HRP-mediated peroxidation of Amplex red to resorufin (red fluorescence) takes place specifically in the DDAB/*trans*-AzoAsp$_2$ droplets, whereas HH-mediated cleavage of a FRET-ssRNA substrate to release a green fluorescence probe is localized within the PDDA/*trans*-AzoAsp$_2$ droplets. **e**,**f**, Time-lapse fluorescence microscopy images (**e**) and corresponding red fluorescence intensity changes with time (**f**) for HRP/H_2O_2-mediated peroxidation in coacervate-based protocell networks. Resorufin (red fluorescence) is produced and retained specifically within the DDAB/*trans*-AzoAsp$_2$ domains. The data represent mean ± s.d. of four replicates. **g**,**h**, Time-lapse fluorescence microscopy images (**g**) and corresponding green fluorescence intensity changes with time (**h**) for HH-min cleavage, and release and retention of the FRET-substrate (green fluorescence) specifically within the PDDA/*trans*-AzoAsp$_2$ domains. The data represent mean ± s.d. of three replicates. **i**, Schematic showing interdroplet transfer of ssDNA within a chain of alternating coacervate-based protocells; migration occurs from the DDAB/*trans*-AzoAsp$_2$ to PDDA/*trans*-AzoAsp$_2$ domains due to increased solubility of the oligonucleotide in the PDDA-containing matrix. Single-stranded DNA is initially sequestered into a single population of DDAB/*trans*-AzoAsp$_2$ droplets before the addition of a suspension of PDDA/*trans*-AzoAsp$_2$ droplets and self-assembly of the regularly interspersed droplet arrays. **j**,**k**, Time-lapse fluorescence microscopy images (**j**) and corresponding red fluorescence intensity changes with time (**k**) showing transfer of TAMRA-ssDNA from DDAB/*trans*-AzoAsp$_2$ droplets (**1**,**3**,**5**) to adjacent PDDA/*trans*-AzoAsp$_2$ domains (**2**,**4**,**6**) located in the same protocell chains; fluorescence intensity values at positions **1**–**6**, and mean fluorescence values for droplets **1**–**6**, are plotted. Scale bars, **b**, 3 μm; **e**, **g**, **j**, 5 μm.

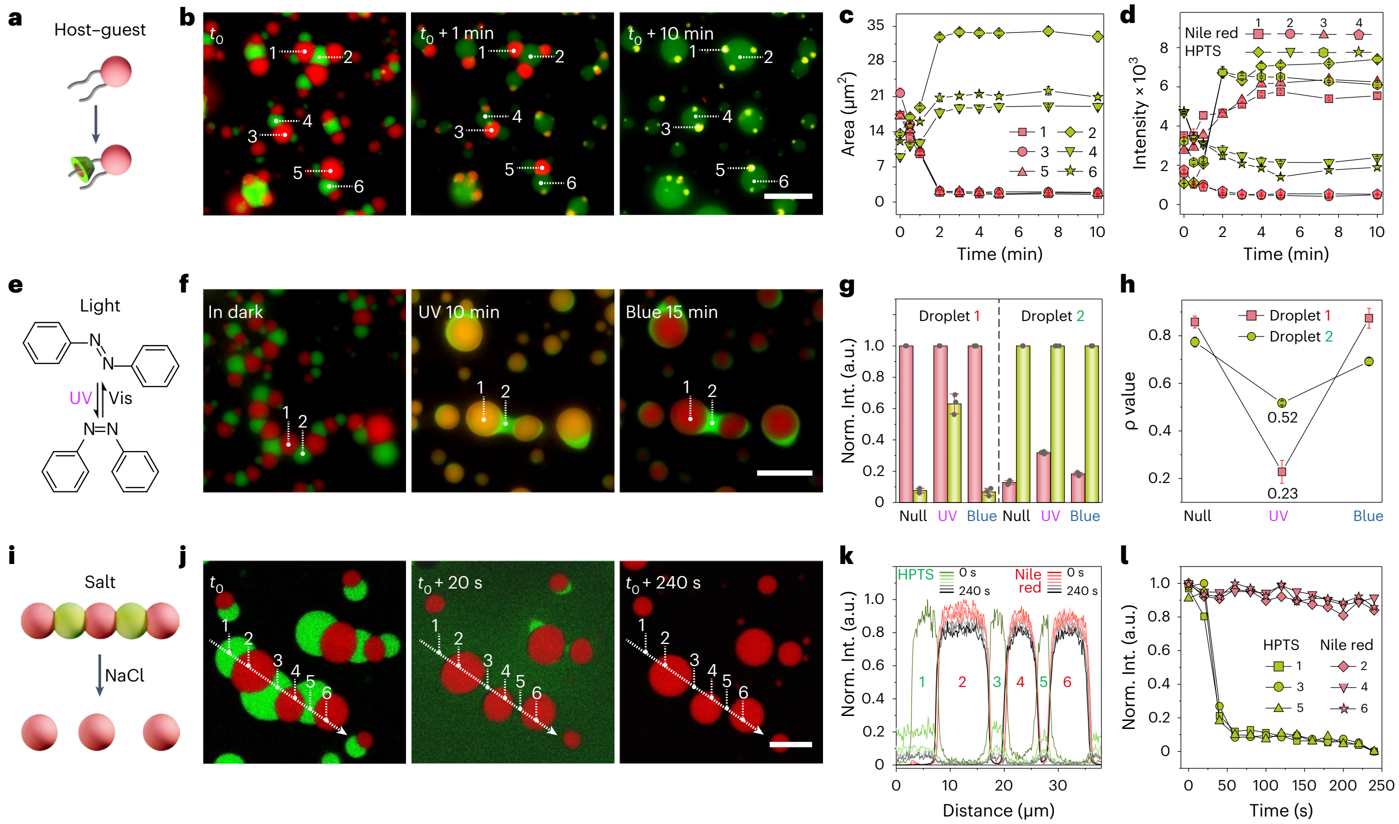

Fig. 5 | Stimuli-induced reconfiguration in protocell networks. a–d, Reconfiguration of protocell networks by β-CD-mediated disassembly of DDAB/*trans*-AzoAsp$_2$ domains (**a**) showing progressive disassociation of Nile red-loaded DDAB/*trans*-AzoAsp$_2$ domains (red) accompanied by local fusion of HPTS-loaded PDDA/*trans*-AzoAsp$_2$ droplets (green) (**b**); and corresponding time-dependent plots of domain sizes and fluorescence intensities for various marked droplets (**c**,**d**). High localized concentrations of HPTS (green) and Nile red (yellow) are observed in the residual DDAB/*trans*-AzoAsp$_2$ droplets 10 min after addition of β-CD ([β-CD]/[DDAB] = 6). **e**–**h**, Reconfiguration of protocell networks by light-mediated *trans*-to-*cis* isomerization of azobenzene (**e**) in internally ordered networks of Nile red-loaded DDAB/*trans*-AzoAsp$_2$ (red) and HPTS-loaded PDDA/*trans*-AzoAsp$_2$ droplets (green). Fluorescence images were recorded after samples were left in the dark (left), 10 min after UV irradiation (middle), or 10 min UV followed by 15 min in blue light (right) (**f**). Corresponding measurements of normalized red and green fluorescence intensities (**g**) and changes in Pearson's correlation coefficient (ρ) (**h**) are also shown. Ultraviolet-induced destabilization results in interdroplet fusion and guest molecular mixing, whereas blue light restores the segregation of Nile red and HPTS. **i**–**l**, NaCl-triggered selective disassembly in protocell networks: the schematic (**i**); fluorescence images of a chain of alternating HPTS-loaded PDDA/*trans*-AzoAsp$_2$ (green, positions **1**,**3**,**5**) and Nile red-loaded DDAB/*trans*-AzoAsp$_2$ (red, positions **2**,**4**,**6**) coacervate droplets before (t_0), and 20 or 240 s after, addition of NaCl showing selective release of HPTS to the environment (**j**); the corresponding line scan (**k**); and time-dependent changes in fluorescence intensities for positions **1**–**6** over a period of 240 s after NaCl addition (**l**). All data represent mean ± s.d. of three replicates. Scale bars, 10 μm.

the protocell networks (Fig. 5). First, as the assembly of the regularly interspersed droplets was dictated by the interplay between different interfacial tensions, we sought to modulate the interdroplet interactions through the adjustment of intermolecular forces specifically within the liquid crystalline DDAB/*trans*-AzoAsp$_2$ domains. To achieve this, we minimized the hydrophobic interactions between the alkyl tails of DDAB by host–guest complexation with β-CD. Addition of β-CD to the protocell networks resulted in progressive disassembly of the DDAB/*trans*-AzoAsp$_2$ droplets over a period of 10 min (Fig. 5a,b and Supplementary Fig. 20a). By contrast, the PDDA/*trans*-AzoAsp$_2$ domains were not disassembled (Fig. 5b and Supplementary Fig. 20b). Measurements of the droplet projected areas were determined by fluorescence microscopy and indicated that the DDAB/*trans*-AzoAsp$_2$ domains typically decreased by 50% from approximately 20 to 10 μm^2 after 1 min of adding β-CD, and were <2 μm^2 in area after 10 min; by contrast, the PDDA/*trans*-AzoAsp$_2$ droplets approximately doubled in area (Fig. 5c). Complete disassembly of the DDAB/*trans*-AzoAsp$_2$ liquid crystalline phase occurred at higher β-CD/DDAB molar ratios (Supplementary Figs. 21 and 22), resulting in release of guest molecules and transfer onto the surface of neighbouring PDDA/*trans*-AzoAsp$_2$ droplets (Fig. 5b,d). Taken together, the results indicate that supramolecular complexation between β-CD and DDAB could be employed to selectively disassemble specific domains of the protocell networks, increase coalescence in the remaining PDDA/*trans*-AzoAsp$_2$ domains and exchange guest molecules between the immiscible coacervate droplets.

We developed a second mechanism of protocell network reconfiguration based on the light-induced *trans*-to-*cis* isomerization of azobenzene within pre-organized chains of the DDAB/*trans*-AzoAsp$_2$ and PDDA/*trans*-AzoAsp$_2$ coacervate droplets (Fig. 5e and Supplementary Figs. 23–26). We reasoned that the reduced hydrophobicity of *cis*-AzoAsp$_2$ would lower the interfacial tension between the DDAB- and PDDA-containing droplets[58], thereby inducing local fusion in the alternating sequence of immiscible droplets in the protocell chains. Density functional theory (DFT) calculations on *trans*- and *cis*-AzoAsp$_2$ (Supplementary Fig. 27), confirmed that the dipole moment of azobenzene increased from 6.64 D (*trans* state) to 44.08 D (*cis* state) after photoisomerization. Experimentally, UV light irradiation of the protocell networks over 10 min gave rise to extensive coalescence of the dissimilar droplets to produce heterogeneous larger droplets with co-localized guest molecules (Fig. 5f and Supplementary Video 4). For

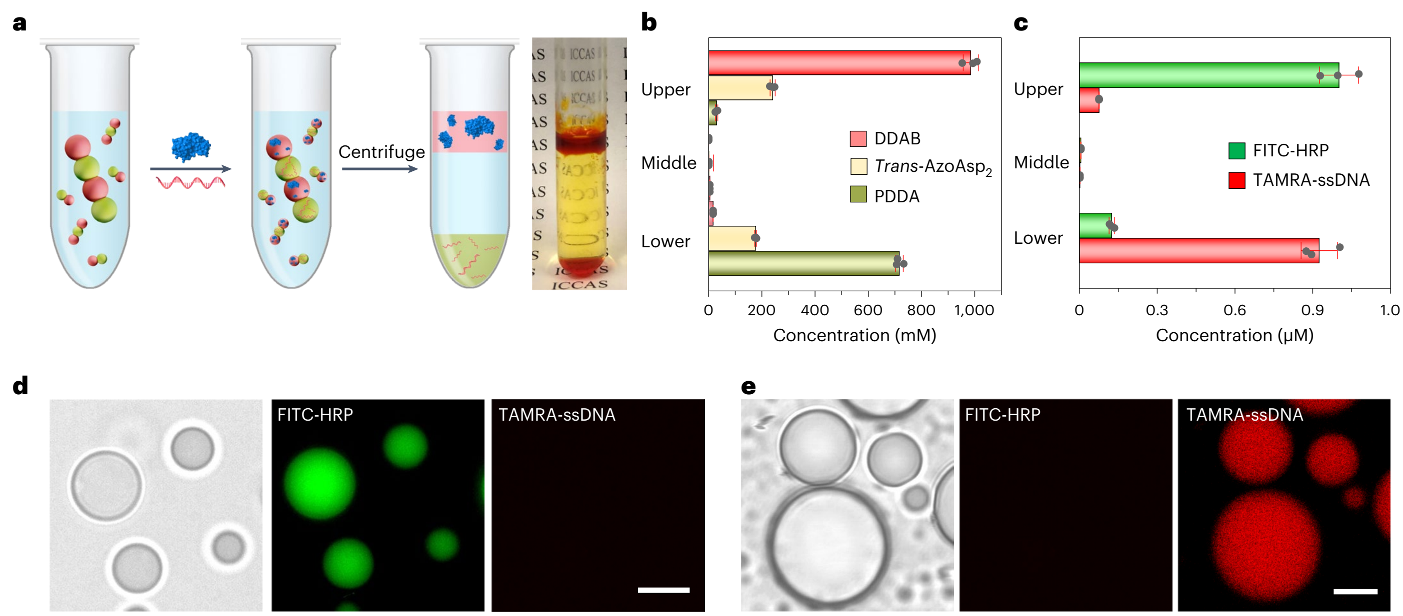

Fig. 6 | Protocell-network-mediated biomolecular extraction and macroscale sorting. a, Selective uptake and spatial segregation of various guest biomolecules in protocell networks comprising an alternating sequence of coacervate droplet domains, followed by centrifugation, results in a lower-density upper layer of DDAB/*trans*-AzoAsp$_2$-enriched coacervate droplets, a dilute aqueous middle layer and a higher-density PDDA/*trans*-AzoAsp$_2$-enriched coacervate droplet lower layer. The partitioned biomolecular cargos are sorted between the upper and lower layers (photograph, far right) according to their selective partitioning in the immiscible coacervate droplets. **b**,**c**, Compositional analysis of coacervate host components by ^{1}H NMR spectroscopy (**b**) and analysis of guest components (FITC-HRP or TAMRA-ssDNA) by fluorescence spectroscopy (**c**) in the three separated layers; the molar ratios of DDAB/*trans*-AzoAsp$_2$ and PDDA/*trans*-AzoAsp$_2$ in the upper and lower layers are close to 4:1 (charge neutralization), and FITC-HRP and TAMRA-ssDNA are efficiently sorted into the DDAB- or PDDA-enriched layers, respectively. All data represent mean ± s.d. of three replicates. **d**,**e**, Optical and fluorescence microscopy images of coacervate droplets obtained from the upper (**d**) or lower (**e**) layers after centrifugation, showing extraction and sorting of FITC-HRP and TAMRA-ssDNA, respectively. Scale bars, 5 μm.

example, co-localization of Nile red and HPTS was monitored by measuring changes in the Pearson's correlation constant (ρ; 0 (correlated), 1 (non-correlation)). Specifically, regions along the protocell chains initially associated with the DDAB/*trans*-AzoAsp$_2$ domains showed a decrease in ρ from approximately 0.88 to 0.22 after photoisomerism, confirming increased levels of spatial overlapping of the Nile red and HPTS fluorophores (Fig. 5g,h). Subsequent irradiation with blue light for 15 min reverted the *cis*-AzoAsp$_2$ isomer back to *trans*-AzoAsp$_2$ as demonstrated by a reestablished ρ value of 0.87 (Fig. 5h). Although demixing of the coacervate phases and resegregation of the guest molecules occurred after exposure to blue light, structural reassembly of ordered multicomponent chains was not observed (Fig. 5f).

As a third approach to chain reconfiguration, we exploited differences in the stability of the DDAB/*trans*-AzoAsp$_2$ and PDDA/*trans*-AzoAsp$_2$ coacervate droplets in aqueous NaCl to selectively disassemble the protocell network (Fig. 5i). Addition of NaCl at concentrations above 2 mM to preformed chains of alternating coacervate droplets dissolved the PDDA/*trans*-AzoAsp$_2$ droplets, releasing encapsulated HPTS, whereas the Nile-red-containing DDAB droplets remained unchanged Fig. 5j–l). The chains remained intact at lower NaCl concentrations (Supplementary Fig. 28).

Protocell network-mediated biomolecular extraction

Having established that internal ordering and selectively biomolecular sequestration could be achieved in chain-like superstructures of immiscible and structurally dissimilar coacervate droplets, we investigated the possibility of exploiting differences in coacervate density to release and separate the interconnected droplets and their constituent biomolecular cargoes (Fig. 6a). To achieve this, we centrifuged suspensions of the protocell arrays at 15,000 × *g*, to produce a stable three-phase system consisting of a DDAB-enriched upper coacervate layer (0.8 vol%), a dilute aqueous middle layer (98.8 vol%) and a PDDA-enriched lower coacervate layer (0.4 vol%). The concentrations for DDAB, PDDA and *trans*-AzoAsp$_2$ in the upper layer were 985, 30 (monomer) and 240 mM, respectively, whereas the lower layer consisted of DDAB (17 mM), PDDA (720 mM; monomer concentration) and AzoAsp$_2$ (177 mM) (Fig. 6b). In both cases, the molar ratios were close to the stoichiometric ratio (4:1) required for near-neutral charge conditions. By contrast, the middle layer contained relatively low levels of DDAB (0.3 mM), PDDA (4.5 mM) and *trans*-AzoAsp$_2$ (0.8 mM), and no coacervate phase (Supplementary Fig. 29). Zeta potential measurements indicated that coacervate droplets present in the upper or lower layers were positively charged (+16 and +33 mV, respectively) (Supplementary Fig. 30).

Given that the adhered microdroplets could be mechanically released from the networks and then separated by differences in density, we used the above procedure as a protocell-based micro-extraction system for selective cargo sequestration and macroscopic sorting. As an initial test, we prepared protocell networks with alternating sequences of DDAB/*trans*-AzoAsp$_2$ and PDDA/*trans*-AzoAsp$_2$ coacervate droplets loaded with FITC-HRP or TAMRA-ssDNA, respectively, and centrifuged the suspensions. Compositional analysis of the separated layers indicated that the guest molecules were retained by their respective coacervate phases after centrifugation, with negligible amounts detected in the aqueous middle layer. Typically, the concentration of FITC-HRP in the DDAB-containing upper layer was approximately eightfold higher than in the PDDA-containing lower layer, whereas the TAMRA-ssDNA concentration in the lower layer was approximately twelvefold higher than that in the upper layer (Fig. 6c). Fluorescence microscopy images of individual coacervate microdroplets extracted from the upper or lower layers confirmed the selective partitioning of the guest biomolecules (Fig. 6d,e). Based on the above results, we used the protocell networks for the biomolecular extraction and macroscale sorting from mixtures of oligonucleotides with polysaccharides (DEAE-dextran/ssDNA), lipids (DiO/ssDNA) or co-factors (ATP/ssDNA), as well as using different dye molecules (Nile red or HPTS) (Supplementary Fig. 31). DEAE-dextran, DiO, ATP and Nile red were partitioned into the DDAB/*trans*-AzoAsp$_2$ coacervate upper layer at approximately 50-, 25-, 20- or 13-fold-higher concentrations than in the PDDA/*trans*-AzoAsp$_2$ lower layer (Supplementary Fig. 32). In contrast, ssDNA and HPTS concentrations in the PDDA-enriched coacervate lower layer after centrifugation were approximately 7-, 20-, 13- or 20-fold higher than observed in the upper layer.

Conclusion

In summary we describe a protocell network based on an interactive self-sorting binary population of immiscible coacervate microdroplets. The membraneless coacervate droplets are produced by associative LLPS and have either liquid-crystalline (DDAB/*trans*-AzoAsp$_2$) or homogeneous (PDDA/*trans*-AzoAsp$_2$) interiors with increased levels of hydrophobicity or hydrophilicity, respectively. Interactions between coacervate droplets with similar structures lead to fusion, whereas contact between structurally disparate droplets results in adhesion. Consequently, heterogeneous aggregates of the dissimilar droplets spontaneously rearrange and self-sort over 60 min into chain-like superstructures with an alternating sequence of liquid crystalline and non-structured coacervate droplet microdomains with hemispherical junctions. This process is facilitated by the reduced dimensionality associated with slow sedimentation of the coacervate droplets and primary aggregates onto pegylated glass coverslips. Thus, increasing the length of the chains and reducing their polydispersity should be possible by implementing greater control over the nucleation and growth kinetics of coacervate droplet adhesion and fusion. By recruiting different biomacromolecules into specific domains of the protocell chains, we exploit the superstructures as a model protocell network capable of macromolecular self-sorting, spatially localized enzyme/ribozyme biocatalysis and interdroplet molecular translocation. We also show that the networks can be topologically reconfigured by using host–guest complexation or salt-induced dissolution to selectively disassemble the DDAB/*trans*-AzoAsp$_2$ domains. Alternatively, photoisomerization of AzoAsp$_2$ by exposure to UV or blue light fuses the immiscible coacervate droplets along the chains and controls the spatial distribution of guest molecules. Finally, as proof-of-concept we develop a protocell network-based micro-extraction and macroscale biomolecular sorting system.

Taken together, the self-assembly of multicomponent coacervate-based protocell superstructures provides a step towards the spontaneous construction of cytomimetic systems with higher-order organization and collective functionality. The networks are thermodynamically self-sorted constructs, being driven by the surface energy minimization of the DDAB/*trans*-AzoAsp$_2$ and PDDA/*trans*-AzoAsp$_2$ droplets in a restraining force-field generated by the local surface adhesion interactions. Currently, the superstructures are structurally stable for at least 30 days at room temperature, and it should be possible to increase their lifetime for example by post-assembly membranization of the coacervate droplets[18–21]. In this regard, preliminary experiments in which the coacervate droplets are coated in a polysaccharide shell to restrict self/self droplet coalescence give rise to extended two-dimensional superstructures containing hundreds of DDAB/*trans*-AzoAsp$_2$ and PDDA/*trans*-AzoAsp$_2$ coacervate droplets arranged in a partially alternating network of compositionally and structurally dissimilar microdomains with hemispherical contact points (Supplementary Fig. 33). It should therefore be possible by judicious modification of the surface chemistry and wetting behaviour to use self-sorting mechanisms to spontaneously assemble protocell superstructures with bespoke levels of interconnectivity. Moreover, manipulating the protocell chains into macroscale networks using microfabricated surfaces or flow chambers could provide an unprecedented approach to the design and construction of artificial multicellular colonies and tissues with embedded circuitry and information processing.

Online content

Any methods, additional references, Nature Portfolio reporting summaries, source data, extended data, supplementary information, acknowledgements, peer review information; details of author contributions and competing interests; and statements of data and code availability are available at https://doi.org/10.1038/s41557-023-01356-1.

References

1. Buddingh, B. C., Elzinga, J. & van Hest, J. C. M. Intercellular communication between artificial cells by allosteric amplification of a molecular signal. *Nat. Commun.* **11**, 1652 (2020).
2. Booth, M. J., Schild, V. R., Graham, A. D., Olof, S. N. & Bayley, H. Light-activated communication in synthetic tissues. *Sci. Adv.* **2**, e1600056 (2016).
3. Tian, L., Li, M., Patil, A. J., Drinkwater, B. W. & Mann, S. Artificial morphogen-mediated differentiation in synthetic protocells. *Nat. Commun.* **10**, 3321 (2019).
4. Gao, N. et al. Chemical-mediated translocation in protocell-based microactuators. *Nat. Chem.* **13**, 868–879 (2021).
5. Adamala, K. P., Engelhart, A. E. & Szostak, J. W. Collaboration between primitive cell membranes and soluble catalysts. *Nat. Commun.* **7**, 11041 (2016).
6. Bhattacharya, A., Cho, C. J., Brea, R. J. & Devaraj, N. K. Expression of fatty acyl-CoA ligase drives one-pot de novo synthesis of membrane-bound vesicles in a cell-free transcription–translation system. *J. Am. Chem. Soc.* **143**, 11235–11242 (2021).
7. Saha, R., Verbanic, S. & Chen, I. A. Lipid vesicles chaperone an encapsulated RNA aptamer. *Nat. Commun.* **9**, 2313 (2018).
8. Marguet, M., Bonduelle, C. & Lecommandoux, S. Multicompartmentalized polymeric systems: towards biomimetic cellular structure and function. *Chem. Soc. Rev.* **42**, 512–529 (2013).
9. Peters, R. J., Louzao, I. & van Hest, J. C. M. From polymeric nanoreactors to artificial organelles. *Chem. Sci.* **3**, 335–342 (2012).
10. Huang, X. et al. Interfacial assembly of protein–polymer nano-conjugates into stimulus-responsive biomimetic protocells. *Nat. Commun.* **4**, 2239 (2013).
11. Li, M., Harbron, R. L., Weaver, J. V., Binks, B. P. & Mann, S. Electrostatically gated membrane permeability in inorganic protocells. *Nat. Chem.* **5**, 529–536 (2013).
12. Torre, P., Keating, C. D. & Mansy, S. S. Multiphase water-in-oil emulsion droplets for cell-free transcription-translation. *Langmuir* **30**, 5695–5699 (2014).
13. Wu, H., Du, X., Meng, X., Qiu, D. & Qiao, Y. A three-tiered colloidosomal microreactor for continuous flow catalysis. *Nat. Commun.* **12**, 6113 (2021).
14. Mukwaya, V. et al. Lectin-glycan-mediated nanoparticle docking as a step toward programmable membrane catalysis and adhesion in synthetic protocells. *ACS Nano.* **14**, 7899–7910 (2020).
15. Mukwaya, V. et al. Programmable membrane-mediated attachment of synthetic virus-like nanoparticles on artificial protocells for enhanced immunogenicity. *Cell Rep. Phys. Sci.* **2**, 100291 (2021).
16. Koga, S., Williams, D. S., Perriman, A. W. & Mann, S. Peptide–nucleotide microdroplets as a step towards a membrane-free protocell model. *Nat. Chem.* **3**, 720–724 (2011).
17. Yewdall, N. A., André, A. A., Lu, T. & Spruijt, E. Coacervates as models of membraneless organelles. *Curr. Opin. Colloid Interface Sci.* **52**, 101416 (2021).

18. Liu, S. et al. Enzyme-mediated nitric oxide production in vasoactive erythrocyte membrane-enclosed coacervate protocells. *Nat. Chem.* **12**, 1165–1173 (2020).
19. Pir Cakmak, F., Marianelli, A. M. & Keating, C. D. Phospholipid membrane formation templated by coacervate droplets. *Langmuir* **37**, 10366–10375 (2021).
20. Gao, N., Xu, C., Yin, Z., Li, M. & Mann, S. Triggerable protocell capture in nanoparticle-caged coacervate microdroplets. *J. Am. Chem. Soc.* **144**, 3855–3862 (2022).
21. Zhang, Y. et al. Giant coacervate vesicles as an integrated approach to cytomimetic modeling. *J. Am. Chem. Soc.* **143**, 2866–2874 (2021).
22. Weitz, M. et al. Diversity in the dynamical behaviour of a compartmentalized programmable biochemical oscillator. *Nat. Chem.* **6**, 295–302 (2014).
23. Sokolova, E. et al. Enhanced transcription rates in membrane-free protocells formed by coacervation of cell lysate. *Proc. Natl Acad. Sci. USA* **110**, 11692–11697 (2013).
24. Dubuc, E. et al. Cell-free microcompartmentalised transcription-translation for the prototyping of synthetic communication networks. *Curr. Opin. Biotechnol.* **58**, 72–80 (2019).
25. Zhu, T. F. & Szostak, J. W. Coupled growth and division of model protocell membranes. *J. Am. Chem. Soc.* **131**, 5705–5713 (2009).
26. Nakashima, K. K., van Haren, M. H., André, A. A., Robu, I. & Spruijt, E. Active coacervate droplets are protocells that grow and resist Ostwald ripening. *Nat. Commun.* **12**, 3819 (2021).
27. Kurihara, K. et al. Self-reproduction of supramolecular giant vesicles combined with the amplification of encapsulated DNA. *Nat. Chem.* **3**, 775–781 (2011).
28. Elani, Y., Law, R. V. & Ces, O. Vesicle-based artificial cells as chemical microreactors with spatially segregated reaction pathways. *Nat. Commun.* **5**, 5305 (2014).
29. Drobot, B. et al. Compartmentalised RNA catalysis in membrane-free coacervate protocells. *Nat. Commun.* **9**, 3643 (2018).
30. Iglesias-Artola, J. M. et al. Charge-density reduction promotes ribozyme activity in RNA–peptide coacervates via RNA fluidization and magnesium partitioning. *Nat. Chem.* **14**, 407–416 (2022).
31. Donau, C. et al. Active coacervate droplets as a model for membraneless organelles and protocells. *Nat. Commun.* **11**, 5167 (2020).
32. Wilson, D. A., Nolte, R. J. & Van Hest, J. C. M. Autonomous movement of platinum-loaded stomatocytes. *Nat. Chem.* **4**, 268–274 (2012).
33. Kumar, B., Patil, A. J. & Mann, S. Enzyme-powered motility in buoyant organoclay/DNA protocells. *Nat. Chem.* **10**, 1154–1163 (2018).
34. Rodríguez-Arco, L., Li, M. & Mann, S. Phagocytosis-inspired behaviour in synthetic protocell communities of compartmentalized colloidal objects. *Nat. Mater.* **16**, 857–863 (2017).
35. Qiao, Y., Li, M., Booth, R. & Mann, S. Predatory behaviour in synthetic protocell communities. *Nat. Chem.* **9**, 110–119 (2017).
36. Qiao, Y., Li, M., Qiu, D. & Mann, S. Response-retaliation behavior in synthetic protocell communities. *Angew. Chem. Int. Ed.* **131**, 17922–17927 (2019).
37. Merindol, R., Loescher, S., Samanta, A. & Walther, A. Pathway-controlled formation of mesostructured all-DNA colloids and superstructures. *Nat. Nanotechnol.* **13**, 730–738 (2018).
38. Villar, G., Graham, A. D. & Bayley, H. A tissue-like printed material. *Science* **340**, 48–52 (2013).
39. Alcinesio, A. et al. Controlled packing and single-droplet resolution of 3D-printed functional synthetic tissues. *Nat. Commun.* **11**, 2105 (2020).
40. Booth, M. J., Restrepo Schild, V., Box, S. J. & Bayley, H. Light-patterning of synthetic tissues with single droplet resolution. *Sci. Rep.* **7**, 9315 (2017).
41. Tian, L. et al. Spontaneous assembly of chemically encoded two-dimensional coacervate droplet arrays by acoustic wave patterning. *Nat. Commun.* **7**, 13068 (2016).
42. Yang, Z., Wei, J., Sobolev, Y. I. & Grzybowski, B. A. Systems of mechanized and reactive droplets powered by multi-responsive surfactants. *Nature* **553**, 313–318 (2018).
43. Dupin, A. & Simmel, F. C. Signalling and differentiation in emulsion-based multi-compartmentalized in vitro gene circuits. *Nat. Chem.* **11**, 32–39 (2019).
44. Ramsay, K., Levy, J., Gobbo, P. & Elvira, K. S. Programmed assembly of bespoke prototissues on a microfluidic platform. *Lab. Chip.* **21**, 4574–4585 (2021).
45. Deshpande, S. et al. Spatiotemporal control of coacervate formation within liposomes. *Nat. Commun.* **10**, 1800 (2019).
46. Gobbo, P. et al. Programmed assembly of synthetic protocells into thermoresponsive prototissues. *Nat. Mater.* **17**, 1145–1153 (2018).
47. Galanti, A. et al. A floating mold technique for the programmed assembly of protocells into protocellular materials capable of non-equilibrium biochemical sensing. *Adv. Mater.* **33**, 2100340 (2021).
48. Liu, J. et al. Hydrogel-immobilized coacervate droplets as modular microreactor assemblies. *Angew. Chem. Int. Ed.* **59**, 6853–6859 (2020).
49. McMullen, A. et al. Self-assembly of emulsion droplets through programmable folding. *Nature* **610**, 502–506 (2022).
50. Gong, J., Tsumura, N., Sato, Y. & Takinoue, M. Computational DNA droplets recognizing miRNA sequence inputs based on liquid–liquid phase separation. *Adv. Funct. Mater.* **32**, 2202322 (2022).
51. Funasaki, N. & Neya, S. Multiple complexation of didecyldimethylammonium bromide and cyclodextrins deduced from electromotive force measurements. *Langmuir* **16**, 5343–5346 (2000).
52. Mu, W. et al. Membrane-confined liquid-liquid phase separation toward artificial organelles. *Sci. Adv.* **7**, eabf9000 (2021).
53. Fraccia, T. P. & Jia, T. Z. Liquid crystal coacervates composed of short double-stranded DNA and cationic peptides. *ACS Nano.* **14**, 15071–15082 (2020).
54. Jing, H. et al. Fission and internal fusion of protocell with membraneless 'organelles' formed by liquid–liquid phase separation. *Langmuir* **36**, 8017–8026 (2020).
55. Fisher, R. S. & Elbaum-Garfinkle, S. Tunable multiphase dynamics of arginine and lysine liquid condensates. *Nat. Commun.* **11**, 4628 (2020).
56. Lu, T. & Spruijt, E. Multiphase complex coacervate droplets. *J. Am. Chem. Soc.* **142**, 2905–2914 (2020).
57. Kaur, T. et al. Sequence-encoded and composition-dependent protein–RNA interactions control multiphasic condensate morphologies. *Nat. Commun.* **12**, 872 (2021).
58. Katzir, I., Haimov, E. & Lampel, A. Tuning the dynamics of viral-factories-inspired compartments formed by peptide–RNA liquid–liquid phase separation. *Adv. Mater.* **34**, 2206371 (2022).

Methods

Preparation of coacervate microdroplets and linear protocell networks

Trans-AzoAsp$_2$ solutions were stored in the dark for at least three days before use to ensure complete isomerization to the *trans* state. First, to prepare DDAB/*trans*-AzoAsp$_2$ coacervate microdroplets, water (28 µl), DDAB (20 µl, 10 mM, pH 8.0) and *trans*-AzoAsp$_2$ (2 µl, 25 mM, pH 8.0) were sequentially mixed to reach a total concentration of 5 mM and molar ratio of 4:1. The freshly prepared microdroplets were incubated for 5 min before use. Second, PDDA/*trans*-AzoAsp$_2$ coacervates were prepared by mixing water (44 µl), PDDA (4 µl, 50 mM, pH 8.0) and *trans*-AzoAsp$_2$ (2 µl, 25 mM, pH 8.0) with the same protocol. Third, to prepare chain-like protocell assemblies, water (22 µl), DDAB (20 µl, 10 mM, pH 8.0), PDDA (4 µl, 50 mM, pH 8.0) and *trans*-AzoAsp$_2$ (4 µl, 25 mM, pH 8.0) were sequentially mixed to reach a total concentration of 10 mM and molar ratio of 2:2:1. The mixture was then incubated for 50 min at room temperature.

Fluorescence recovery after photobleaching

Fluorescence recovery after photobleaching experiments were conducted on a Nikon A1RSi using a ×100 oil immersion lens. For RITC-BSA-containing DDAB/*trans*-AzoAsp$_2$ coacervate droplets, circular regions of interest (ROIs, 2.0 µm) were bleached with a 561 nm laser over 125 ms at 100% power. For RITC-BSA-loaded PDDA/*trans*-AzoAsp$_2$ droplets, the ROIs (2.5 µm) were bleached with a 561 nm laser over 125 ms at 100% power. For DiO-loaded DDAB/*trans*-AzoAsp$_2$ coacervate droplets, the ROIs (2.0 µm) were bleached with a 488 nm laser over 250 ms at 100% power. For RITC-PDDA-loaded PDDA/*trans*-AzoAsp$_2$ droplets, the ROI (2.0 µm) was bleached with a 561 nm laser over 250 ms at 100% power. The fluorescence recovery of the bleached areas was all recorded over a period of 60 s. For Nile-red-containing DDAB-rich domains within microdroplet clusters, the ROIs (6.5 µm) were bleached with a 561 nm laser over 2 s at 20% power; subsequent fluorescence recovery of the bleached area was recorded over a period of 900 s. For HPTS-loaded PDDA-rich domains within microdroplet clusters, ROIs (2.5 µm) were bleached with a 488 nm laser over 2 s at 5% power; subsequent fluorescence recovery of the bleached area was recorded over a period of 900 s. The fluorescence intensity of the bleached area was background subtracted, normalized to the fluorescence intensity of the first postbleach image, corrected for acquisition bleaching using a similarly sized reference droplet in the frame, and normalized to the mean prebleach intensity. The FRAP recovery curve was averaged from three droplets.

Horseradish-peroxidase-mediated peroxidation within DDAB/*trans*-AzoAsp$_2$ subdomains

Typically, 5 µl of hydrogen peroxide (150 µM) was added to 50 µl of a protocell network dispersion with encapsulated HRP (2 µg ml^{-1}) and Amplex red (15 µM). The emission intensity of the product resorufin was monitored using a confocal laser scanning microscopy (CLSM) over 600 s.

Ribozyme-mediated catalysis within PDDA/*trans*-AzoAsp$_2$ subdomains

Typically, 0.5 µl of hammerhead ribozyme derived from satellite RNA of tobacco ringspot virus (HH-min, 50 µM) was added to 50 µl of a protocell network suspension (DDAB/PDDA/*trans*-AzoAsp$_2$ = 4 mM /4 mM/2 mM) along with the encapsulated FRET-substrate (0.2 µM). The mixture was incubated at room temperature and the cleavage of the FRET-substrate strand by HH-min was monitored by the enhancement of fluorescein emission at 500–550 nm, associated with the increase in the distance between FAM and Black Hole quencher 1. The fluorescence recovery was also monitored on a CLSM over 540 min. The sequences of HH-min and FRET-substrate are shown in Supplementary Table 2.

β-CD-triggered reconfiguration of protocell networks

A desired amount of β-CD solution (15 mM, pH 8.0), for example, 80 µl, was added to 50 µl of a protocell network suspension prepared with encapsulated Nile red and HPTS at varying β-CD/DDAB molar ratios. The corresponding fluorescence microscopy images were analysed to obtain the area fluorescence intensity of the DDAB- and PDDA-enriched domains using Fiji-ImageJ.

Light-modulated reconfiguration of protocell networks

Trans/*cis*-AzoAsp$_2$ isomerization was achieved with ultraviolet (365 nm, 30 W light-emitting diode light) and blue light (450 nm, 20 W high-intensity discharge lamp) irradiation. For ^{1}H NMR characterization, 0.6 ml of *trans*-AzoAsp$_2$ solution (6 mM in dimethyl sulfoxide (DMSO)-d_6) was used. *Trans*-to-*cis* isomerization was obtained with UV light irradiation for 90 min, whereas *cis*-to-*trans* isomerization was induced after irradiation with blue light for 60 min (Supplementary Table 3). Isomerization of AzoAsp$_2$ (0.6 mM in water) was also investigated on a UV–vis spectrophotometer with 300 s UV and 300 s blue light irradiation. Light-induced transformation of protocell networks was achieved on an optical microscope with UV ($325 < \lambda < 375$ nm, 120 W short-arc mercury light source) and blue light ($460 < \lambda < 500$ nm, 120 W short-arc mercury light source) irradiation.

Determination of Pearson's correlation constant

To assess the colocalization of Nile red and HPTS within DDAB- and PDDA-enriched coacervate domains following light irradiation, the corresponding fluorescence microscopy images were analysed to obtain the normalized red (Nile red) and green (HPTS) fluorescence intensities using Fiji-ImageJ. The Pearson's correlation coefficient ρ was determined using the following equation:

$$\rho = \frac{|\mathrm{Fl}\,(\mathrm{red}) - \mathrm{Fl}\,(\mathrm{green})\,|}{\mathrm{Fl}\,(\mathrm{red}) + \mathrm{Fl}(\mathrm{green})}$$

where $\mathrm{Fl}_{(\mathrm{red})}$ was the normalized red fluorescence intensity, and $\mathrm{Fl}_{(\mathrm{green})}$ the normalized green fluorescence intensity.

Biomolecular extraction via macroscale sorting

Typically, 20 µl of a fluorophore mixture, for example, FITC-HRP (7 µM, 10 µl, in 10 mM PBS)/TAMRA-ssDNA (1 µM, 10 µl, in 10 mM PBS); RITC-DEAE-dextran (0.3 mg ml^{-1}, 10 µl, in 10 mM PBS)/FAM-ssDNA (0.03 mg ml^{-1}, 10 µl, in 10 mM PBS); DiO (1 µM, 10 µl, in DMSO)/TAMRA-ssDNA (1 µM, 10 µl, in 10 mM PBS); TNP-ATP (1 µM, 10 µl, in 10 mM PBS)/TAMRA-ssDNA (1 µM, 10 µl, in 10 mM PBS) or Nile red (100 µM, 10 µl)/HPTS (100 µM, 10 µl) were added to a suspension of the protocell networks (770 µl) in Eppendorf tubes. The mixtures were centrifuged at 15,000 × *g* for 15 min, and the upper (DDAB-rich) and lower (PDDA-rich) phases were redispersed in 150 µl NaCl solution (5 M), resulting in coacervate disassembly. The DiO- and Nile-red-containing DDAB-rich upper phase were disintegrated by DMSO and MeOH, respectively. The fluorescence intensity of the upper (DDAB-rich) or lower (PDDA-rich) phase was then recorded using a microplate reader (CLARIOstar Plus).

Spontaneous assembly of two-dimensional protocell superstructures

DDAB (20 µl, 2.5 mM, pH 8.0), PDDA (4 µl, 12.5 mM, pH 8.0) and *trans*-AzoAsp$_2$ (4 µl, 6.25 mM, pH 8.0) were sequentially mixed to reach a total concentration of 4.5 mM and molar ratio of 2:2:1. Nile red (1 µl, 10 µM) and HPTS (1 µl, 30 µM) were subsequently added. The mixture was then incubated for 15 min in the Eppendorf tube, followed by addition of dextran (2 µl, 0.5 mg ml^{-1}, 155 kDa). The dispersion was poured into a sample cell, allowed to settle for 60 min and monitored by CLSM.

Density functional theory calculations

NWChem was used for the quantum chemical calculation[59]. Similar to literature reports[60,61], DFT calculations used the B3LYP exchange-correlation and 6−31 G basis set. The solvent effect was considered by using a conductor-like screening model (COSMO)[62]. The dielectric constant used for water was 78.4. The atomic radii were taken from previous studies[63]. Electron-rich and electron-poor potentials are labelled red and blue, respectively, in the electrostatic potential plots.

Small- and wide-angle X-ray scattering

Small- and wide-angle X-ray scattering experiments were undertaken at room temperature on a Ganesha system 380 (SAXSLAB) equipped with multilayer-focused copper K_a radiation as the X-ray 381 source (Genix 3D Cu ULD). A semiconductor with silver behenate was used for the small-angle region and LaB_6 for the wide-angle region. The DDAB/*trans*-AzoAsp$_2$ and PDDA/*trans*-AzoAsp$_2$ coacervate dispersions were centrifuged at 9,390 × g for 15 min, and the water phase was discarded. The coacervate phase was collected for SAXS and WAXS analysis. The scattering intensity of a colloidal dispersion, $I(q)$, is given as a function of the momentum transfer:

$$I(q) = (\rho_p - \rho_s)^2 V_p \varnothing_p P(q) S(q)$$

where ρ_p and ρ_s are the contrast of the colloidal particle and media, respectively, V_p is the volume of the colloidal particle, $\varnothing_p$ is the volume fraction of colloidal particle, $P(q)$ is the form factor and $S(q)$ is the structure factor. The scattering patterns were recorded on an imaging-plate with $q = 4\pi \sin\theta/\lambda$, where λ is the wavelength (0.1542 nm) and 2θ is the scattering angle. The interplanar spacing (d) was calculated according to Bragg's law, $d = 2\pi/q$.

Data availability

All data supporting the findings of this study are available within the article and its Supplementary Information, and from the corresponding authors on reasonable request. Source Data are provided with this paper.

References

59. Valiev, M. et al. NWChem: a comprehensive and scalable open-source solution for large scale molecular simulations. *Comput. Phys. Commun.* **181**, 1477–1489 (2010).
60. Rego, L. G. C. & Bortolini, G. Modulating the photoisomerization mechanism of semiconductor-bound azobenzene-functionalized compounds. *J. Phys. Chem. C* **123**, 5692–5698 (2019).
61. Benmensour, M. A. et al. Azobased iminopyridine ligands and their rhenium metal complexes: syntheses, spectroscopic, *trans*–*cis* photoisomerization and theoretical studies. *J. Photoch. Photobio. A* **368**, 78–84 (2019).
62. Klamt, A. & Schüürmann, G. COSMO: a new approach to dielectric screening in solvents with explicit expressions for the screening energy and its gradient. *J. Chem. Soc. Perkin Trans.* **2**, 799–805 (1993).
63. Stefanovich, E. V. & Truong, T. N. Optimized atomic radii for quantum dielectric continuum solvation models. *Chem. Phys. Lett.* **244**, 65–74 (1995).

Acknowledgements

This work was supported by the Strategic Priority Research Program of the Chinese Academy of Sciences (grant no. XDB0480000) to Y.Q., the National Natural Science Foundation of China (grant nos. 22272183 and 22072159 to Y.Q., and 22172007 to Y.L.), the Science Fund for Creative Research Groups of the National Natural Science Foundation of China (grant no. 52221006) to Y.L., and the Fundamental Research Funds for the Central Universities (grant nos. buctrc202015 and PT2208 to Y.L). S.M. was funded by the ERC Advanced Grant Scheme (grant no. EC-2016-674 ADG 740235).

Author contributions

W.M. and L.J. performed the experiments and analysed the data. M.Z. and J.W. performed computational experiments. Y.Q. led the project. Y.L., S.M. and Y.Q. conceived, designed and supervised the study, analysed the data and wrote the manuscript. All authors discussed the results and commented on the manuscript.

Competing interests

The authors declare no competing interests.

Additional information

Supplementary information The online version contains supplementary material available at https://doi.org/10.1038/s41557-023-01356-1.

Correspondence and requests for materials should be addressed to Yiyang Lin, Stephen Mann or Yan Qiao.

Peer review information *Nature Chemistry* thanks the anonymous reviewers for their contribution to the peer review of this work.

Reprints and permissions information is available at www.nature.com/reprints.